POLISH MARITIME RESEARCH 1 (129) 2026 Vol. 33; pp. 4-13
10.2478/pomr-2026-0001

Numerical Simulation of Ship Resistance and Ice Load Distribution in Pack Ice

Bin Mei *
Jiayun Ye
Yujia Zhang
Congcong Zhao
Guoyou Shi
School of Navigation, Dalian Maritime University, Dalian, China

* Corresponding author: *meibindmu@163.com (Bin Mei)*

ABSTRACT

With global warming enhancing the navigability of Arctic routes, the accurate prediction of ice resistance during navigation is of great engineering significance for the design and performance evaluation of polar ships. This study proposes a high-fidelity numerical simulation method that combines image recognition with CFD–DEM coupling and a six-degree-of-freedom (6-DOF) dynamic model to predict ship resistance in pack ice conditions. Using ice images from the CEHINAV towing tank experiments in Spain, the watershed image segmentation algorithm was applied to extract the spatial distribution and size information of ice blocks. A digital ice field was then reconstructed by surface injection of ice fragments of various sizes, thereby achieving consistency with the physical ice field. In the fluid–structure interaction simulations, a dynamic overset mesh and 6-DOF motion model were introduced to realistically reproduce the ship's motion and the ship–ice interactions in the pack ice zone. Numerical simulations under different speeds and ice concentrations show that the average deviation from experimental data remains within 10%, thus confirming the accuracy and reliability of the proposed method. The results indicate that the bow region is the main area of ice loading and resistance concentration, with resistance increasing significantly as the ice concentration rises. The resistance curves exhibit evident nonlinear fluctuations and unloading phenomena. Further regional analysis reveals that the transverse resistance distribution along the hull gradually decreases from the midship toward both sides, while local regions exhibit transient fluctuations, a finding that highlights the complex and unsteady characteristics of ship–ice interactions.

Keywords: ice resistance; overset grid; CFD–DEM; ice load distribution

INTRODUCTION

In recent years, global warming has led to continuous shrinkage of polar ice caps, with increasingly significant summer sea ice melt [1]. This change has created unprecedented opportunities for Arctic shipping and resource exploration. In this context, the commercial value of Arctic routes and the ongoing development of polar resources have driven a rapid increase in ship traffic in polar waters [2]. The Northern Sea Route and Northwest Passage are of particular interest, due to their potential to greatly shorten Asia–Europe transit distances, while the region's rich oil, gas, mineral, and biological resources continue to attract international research and investment efforts [3]. However, polar navigation still involves many challenges, including extreme low temperatures, limited visibility, communication difficulties, and complex ice conditions [4], with sea ice-induced resistance being one of the most critical factors [5]. This resistance affects propulsion power requirements, fuel efficiency, and speed control, and is a vital aspect of navigational safety.

Hence, accurate prediction of ice resistance is of significant engineering value for the design and operation of polar ships.

Current approaches to ice resistance prediction mainly rely on three methods: testing of ship models, semi-empirical formulas, and numerical simulations. Ship model tests reproduce scaled conditions in controlled environments, and offer a high level of reliability. For example, Gutierrez-Romero et al. [6] used towing tank tests to examine the influence of ice concentration and speed on ship resistance, whereas Matala et al. [7] used brash ice channel tests to study the effects of ice concentration and channel width, validating the results against full-scale data, and Suominen et al. [8] proposed a revised friction coefficient for freshwater brash ice, with improved model test accuracy. These studies show that ship model testing provides valuable references for brash ice navigation research. However, such tests are expensive, time-consuming [9], and limited in terms of revealing detailed mechanisms, especially under complex or mixed ice conditions where data acquisition and analysis are constrained. As an alternative, semi-empirical approaches can be used, such as the model proposed by Lindqvist in which ice resistance is decomposed into three components: breaking resistance, frictional resistance, and piling-up resistance [10]. This type of model is commonly used for the preliminary evaluation of designs, but its applicability is limited to specific hull forms and ice conditions, making this approach less suitable for detailed assessments in variable ice environments.

Following recent advances in computing, numerical simulations have shown strong advantages in regard to modelling complex ice conditions and ship–ice interactions. Numerical and experimental methods now form a complementary research framework [11], and represent flexible and efficient tools for evaluating the performance of a ship in ice. In brash ice simulations, computational fluid dynamics coupled with the discrete element method (CFD–DEM) is used for its ability to capture both the discrete nature of ice and the continuous behaviour of fluids. Although idealised ice shapes are often adopted for reasons of computational efficiency, block-type models (e.g. rectangles or cubes) are better able to represent real floe breakage behaviour. Kim et al. [12] established a ship–ice interaction model based on triangular discrete element method (DEM) ice particle clusters, and systematically analysed the resistance characteristics of an icebreaking cargo vessel in dense pack ice conditions. Gutierrez-Romero et al. [6] applied rectangular blocks in model tests to study resistance, while Huang et al. [13] used ITTC-standard pre-sawn parallelogram ice, and reported simulation errors of within 10% of the test data. Geometric fidelity at this level allows for accurate reproduction of the key interactions, including floe rotation, rolling upon impact, and complex multi-point contact with the hull [14]. The use of block-shaped ice models, such as rectangular or cubic shapes, can realistically reflect ship–ice interactions and multi-point contact characteristics.

Studies have confirmed that CFD–DEM modelling provides accurate and practical solutions for performance evaluation, ice load prediction, and resistance analysis. For instance, Xie et al. [15] simulated the resistance of a polar merchant ship in brash ice, and accurately predicted power and ice load distribution. Zhang et al. [16] investigated full-scale ship–ice interactions under FSICR ice conditions, and verified the accuracy and applicability of their model for prediction of ice resistance and reproduction of the contact process. Tang et al. [17] reported a high level of agreement between simulations and tests for the KRISO container ship, with the impact and accumulation of bow ice identified as the main sources of resistance. These findings demonstrate the strong predictive capabilities of this method for complex ship–ice interactions in pack ice environments. However, most simulations still use dynamic ice injection (e.g. [15-17]), in which the motion of the ice is driven by water flow, unlike real icebreaking operations, which causes systematic deviations in peak resistance and accumulation behaviour, thus reducing the accuracy.

This study presents a coupled simulation method for dynamic ship navigation in pack ice, and introduces a novel DEM-based surface injection technique. Using experimental data from the CEHINAV towing tank in Spain [6], a digital pack ice field was constructed to replicate the distribution of the ice, including its position and size. This approach overcomes the limitations of the traditional static ship/moving ice method by coupling dynamic overset grids with a six-degree-of-freedom (6-DOF) model to simulate ship motion.

NUMERICAL MODEL

This section presents a detailed description of the modelling process used in the numerical simulations, including the setup of the ship model, parameterisation of the ice particles, generation of the pack ice field, and configuration of the computational domain. The proposed modelling framework provides a comprehensive basis for investigating the mechanisms of ship–ice interaction.

SHIP MODEL

Accurate parameterisation of the ship model is the primary step in building the numerical simulation framework. In this study, the polar research vessel B.I.O. Hespérides, operated by the Spanish Navy [6], is selected as the reference model. A scale model in the ratio 1:21.43 is used. The principal particulars of the model are listed in Table 1.

Table 1. Main details of the full-scale and model ships

Parameter	Full-scale ship	Scale model
Length (m)	82.588	3.854
Beam (m)	14.591	0.681
Draft (m)	4.421	0.207

In this vessel, an icebreaking bow design is adopted that strikes a balance between icebreaking capability and seakeeping performance in open water. According to the publicly available information on the official platform of

PolarIN (EU Polar Research Infrastructure Network), the vessel is classified as Ice Class 1C [18], making it suitable for navigation in ice-infested open seas [19].The test data for the ship model are derived from the Gutierrez-Romero research team [6]. The line plan of the ship model in Fig. 1 illustrates the shape of the waterlines and the curvature characteristics of the hull surface, in detail. Based on this line plan, a numerical model was constructed, as depicted in Fig. 2, which will be employed in the subsequent numerical simulations.

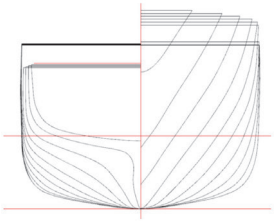

Fig. 1. Body plan

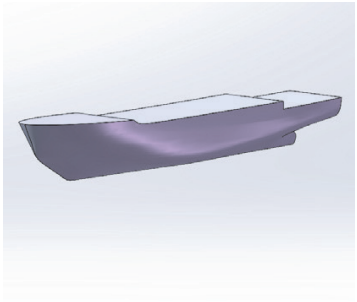

Fig. 2. Ship model

ICE PARTICLES

To ensure realistic replication of the navigation of the ship model in a pack ice environment, an ice particle model was constructed based on the physical properties of paraffin wax, following the measured data from ship model tests conducted in the CEHINAV towing tank [6]. The ice particles were rectangular blocks with a uniform thickness of 40 mm. According to the experimental observations, the pack ice consisted of two distinct size categories, with the small floes measuring one-quarter the size of the large ones. The specific parameters are listed in Table 2, and the geometric model of the ice particles is shown in Fig. 3.

Table 2. Properties of ice particles

Physical parameter	Value
Ice Young's modulus(Pa)	8×107
Ice density(kg/m^3)	830
Ice Poisson's ratio	0.45
Large ice block (Length (mm) × Width (mm))	484×295
Small ice block (Length (mm) × Width (mm))	242×148
Ice block thickness (mm)	40

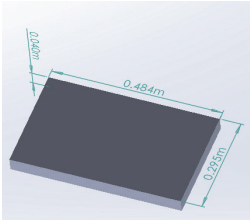

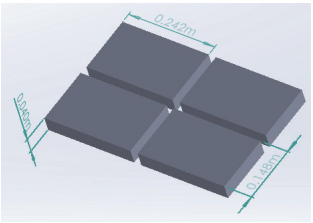

(a) Large ice block *(b) Small ice blocks*

Fig. 3. Geometric model of the ice blocks

CONTACT MODEL

The interactions between the ice blocks and between the ice and the ship hull were modelled using DEM. The Hertz–Mindlin contact model [20] was adopted in this study, as shown in Fig. 4.

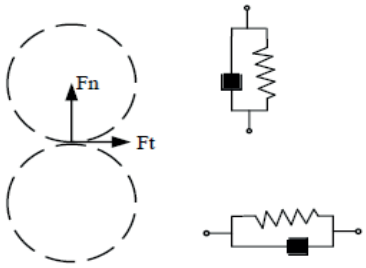

Fig. 4. Particle contact model

Due to the nonlinear elastic contact and damping characteristics, the contact force between particles includes a normal force and a tangential force, expressed as shown in Eq. (1):

$$F_{contact} = F_n n + F_t t \tag{1}$$

where the normal force F_n and tangential force F_t depend on the contact overlap between particles, the material parameters (such as the equivalent elastic modulus and shear modulus), and the restitution coefficients. The actual parameter settings are given in Table 3. Compared with linear models, this model more realistically reflects the nonlinear stiffness characteristics and energy dissipation behaviour of ice fragment collisions.

IDENTIFICATION AND GENERATION OF PACK ICE

Fig. 5 illustrates the particle distribution patterns corresponding to three different pack ice concentrations (30%, 45%, and 60%), as observed in the ship model experiments.

(a) Pack ice at 30% concentration

(b) Pack ice at 45% concentration

(c) Pack ice at 60% concentration

Fig. 5. Pack ice with varying concentrations

In Fig. 6, the image segmentation results are presented for the ice field with 30% concentration. The blue lines in the figure represent auxiliary positioning lines generated by the algorithm, whose intersection points correspond to the geometric centres of individual ice fragments and characterise the spatial distribution of ice pieces within the computational domain [21]. After processing of the ice field image using the watershed image segmentation algorithm, identification and spatial localisation of ice particles were successfully achieved.

The watershed image segmentation algorithm is a region segmentation method based on the principles of mathematical morphology and topological terrain analysis. The main concept of this approach is to regard a greyscale image as a topographic surface, where the pixel greyscale values correspond to elevation. The algorithm simulates the process of 'water convergence': as the water level gradually rises from local minima, different 'catchment basins' are successively submerged. When the flows of water from different basins meet, 'watershed lines' are formed, thereby achieving precise segmentation between adjacent regions.

This method ensures both boundary closure and morphological integrity, while achieving high-precision segmentation and centre localisation of ice fragments, thus providing reliable input data for geometric modelling and numerical simulation of the ice field.

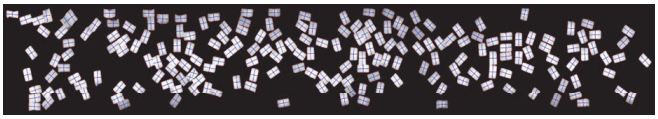

Fig. 6. Image segmentation of pack ice at 30% concentration

In this study, a surface injector technique is adopted to construct the broken ice field. Ice particles are released along a three-dimensional boundary surface following a realistic spatial distribution, thereby overcoming the limitations of conventional grid- or point-based injectors in terms of representing spatial heterogeneity. The method is coupled with a two-way DEM–CFD framework to resolve the real-time interaction between ice particles and the surrounding fluid: DEM is used to handle the ship–ice contact dynamics, while the CFD module captures the hydrodynamic effects.

Compared with other injection approaches [15-17], the surface injector provides a higher level of spatial freedom, enabling precise control over the timing of particle release, and the positions and size distribution of the particles. This allows for nonlinear behaviours of the broken ice, such as sliding and rotation, to be effectively reproduced, and offers significant advantages in regard to simulating the dynamic bow–ice interaction region. Through matching with physical experimental data and applying a watershed-based image segmentation algorithm, the spatial distribution of the floes extracted from the images is used to drive the surface injector to generate ice particles at the corresponding locations, as shown in Fig. 7, thereby achieving a balance between generation efficiency and scene fidelity.

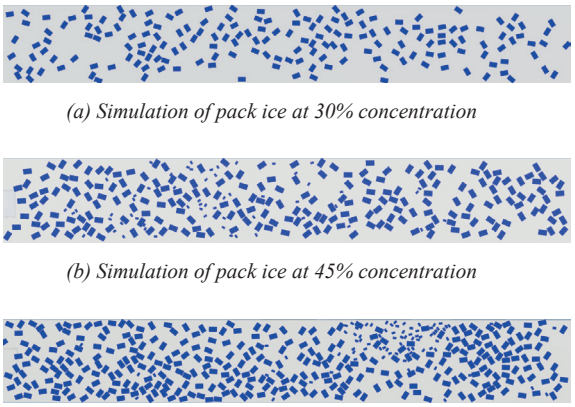

(a) Simulation of pack ice at 30% concentration

(b) Simulation of pack ice at 45% concentration

(c) Simulation of pack ice at 60% concentration

Fig. 7. Simulations of pack ice at varying concentrations

The classification of pack ice concentration follows conventional standards described in Bowditch [22] and CCG [23], where 'very open pack' corresponds to 10–30% coverage and 'open pack' to 40–60% coverage. The concentrations chosen here therefore correspond to 'very open' to 'open' pack ice; these levels are consistent with the physical experiments and allow for validation of the proposed CFD–DEM numerical framework against available model test data. Future studies may consider higher ice concentrations to investigate the performance of ships under more extreme ice conditions.

COMPUTATIONAL DOMAIN AND MESHING

The establishment of the computational domain is a critical step in numerical simulation methods, as the quality of the computational mesh directly determines the accuracy of the numerical results. The computational domain and mesh configuration selected in this case are shown in Fig. 8. In this study, a trimmed cell mesher was applied to generate the mesh outside the overset region, while a trimmed cell mesher, prism layer mesher, and surface remeshing techniques were employed within the overset region.

The computational domain was defined as a rectangular region with dimensions of 33 × 10 × 3.9 m, and was designed to simulate the floating ice environment. Pressure outlet boundary conditions were applied to the top, sides, and outlet boundaries, while the bottom surface was modelled as a wall. To simulate the relative motion of the ship through the ice region, a dynamic fluid body interaction (DFBI) model was adopted for free body motion, and an overset region was established around the hull to refine the local mesh and enable dynamic mesh interaction between the ship and the background domain.

The base mesh size was set to 0.5 m. A total of five prism layers were applied, with an overall thickness of 0.01 m, extending to 1.5 times the base cell height. Local mesh refinement was performed in the ice region, using the trimmed cell mesher to generate anisotropic grids. The mesh size in the X and Y directions was refined to 10% of the base size, and 6% in the Z direction. Partial refinement was also applied to the surrounding water in the vicinity of the ship

and the pack ice contact zone, with the mesh size reduced to 6% of the base size for improved accuracy. To take into account the ship–ice interactions, further refinement was applied around the hull using surface remeshing, with the mesh size reduced to 3% of the base size. An overset mesh was generated around the ship to ensure accurate representation of the ship's motion. At the end of the mesh generation stage, a total of 1,758,642 cells were obtained.

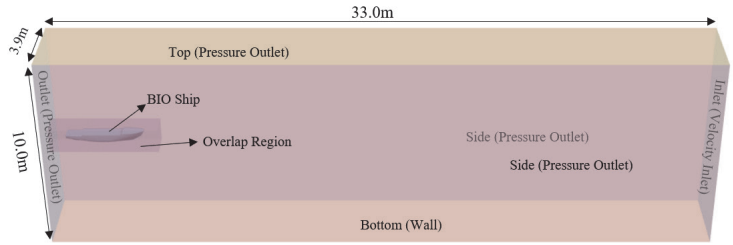

(a) Computational domain

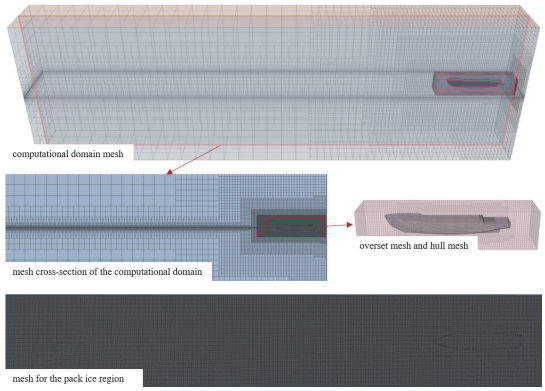

(b) Cross-section of the mesh for the computational domain

Fig. 8. Computational domain and computational mesh

VALIDATION OF THE NUMERICAL METHOD

EXPERIMENTAL SETUP

Tests were conducted under various pack ice concentration levels and vessel speeds. For the cases with 45% and 60% concentration, ice pieces of two different sizes were used, whereas only large ice pieces were employed for the 30% concentration. The main parameters used in the simulation are listed in Table 3.

Table 3. Main parameters for the simulation

Parameter	Value
Water density (kg/m3)	1000
Ice–ship restitution coefficient	0.5
Ice–ice restitution coefficient	0.25
Ice–ship friction coefficient	0.25
Ice–ice friction coefficient	0.1
Time step (s)	0.01
Pack ice concentration (%)	30, 45, 60
Velocity (m/s)	0.22, 0.33, 0.53

RESISTANCE ERROR ANALYSIS

To verify the accuracy of the numerical simulation, the results were compared with those of the ship model tests, and the relative errors were calculated as shown in Table 4. The results indicate that the relative errors under all conditions are within 10%, with most falling between 3% and 7%, representing good agreement. In particular, the smallest errors occur under the 45% concentration condition (ranging from 3.96% to 7.45%), while slightly larger errors are observed under the 30% and 60% concentration conditions. Overall, the model yields more stable performance at medium to high speeds (e.g. 0.53 m/s), indicating good predictive capability.

Table 4. Values of average ship resistance obtained from ship model tests at various speeds and pack ice concentrations

Velocity (m/s)	Concentration (%)	Numerical simulation results (N)	Ship model test results (N)	Relative error (%)
0.22	30	2.586	2.746	5.83
	45	4.992	5.394	7.45
	60	9.767	10.174	4.00
0.33	30	4.571	4.884	6.39
	45	9.223	9.689	4.81
	60	17.502	18.142	3.52
0.53	30	6.329	6.551	3.39
	45	14.191	14.369	1.24
	60	20.548	21.927	6.29

The relationship between the average resistance and the pack ice concentration shows a clear increasing trend, as illustrated in Fig. 9. At a given sailing speed, the average resistance at 60% concentration is approximately three to

four times higher than at 30% concentration. This finding is consistent with the conclusions of ship model tests conducted by Huang et al. [24], which indicated that the pack ice concentration is the primary factor influencing ice resistance.

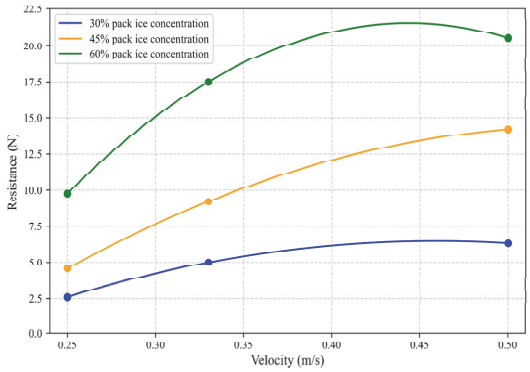

Fig. 9. *Mean ship resistance across different ice concentrations*

In summary, the CFD numerical simulation method developed in this study yields high accuracy under various ice concentrations and sailing speeds. It effectively reproduces the variation trends in the resistance observed in experiments, and exhibits strong engineering applicability and significant potential for broader adoption.

ANALYSIS OF RESULTS

RESISTANCE ANALYSIS

When navigating through pack ice regions, a ship experiences resistance mainly due to the complex interactions between the hull and pack ice. This includes pushing resistance that arises from the bow pushing aside pack ice, as well as frictional ice resistance due to ice floes sliding along the hull surface.

From the resistance–time (*R–t*) curves shown in Fig. 10, it can be seen that when the ship advances at 0.53 m/s, the resistance fluctuates within the ranges of 0–64 N for 30% ice concentration, 0–110 N for 45%, and 0–206 N for 60%. As the concentration of pack ice increases, the fluctuation amplitude of the R–t curve becomes more pronounced due to the higher frequency of ship–ice contacts, as shown in Fig. 11. At 30% ice concentration, the ice floes are more widely spaced, resulting in few contacts and smaller resistance fluctuations at a speed of 0.53 m/s.

In addition, the sliding or sudden detachment of ice floes from the hull can cause an abrupt drop in ice resistance, a phenomenon known as ice resistance unloading. This is reflected in the resistance curve as a sharp drop or trough, which typically occurs after a peak and is characterised by suddenness and short duration (see Fig. 10(c)), and is especially noticeable at low ice concentrations.

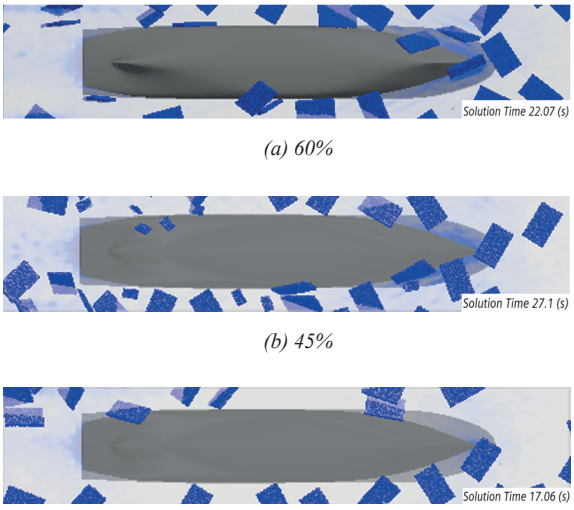

(a) 60%

(b) 45%

(c) 30%

Fig. 11. Ice contact count at the hull bottom for varying ice concentrations

Fig. 12 shows the upper envelope of the ship model's resistance when navigating the ice field at a speed of 0.33 m/s. Significant peaks in the resistance curve typically originate from instantaneous frontal collisions between the ship bow and pack ice. The resistance peaks under 60% ice concentration are notably higher than those at 30% and 45%; this is because the ship hull has difficulty effectively clearing the ice ahead during navigation, causing pack ice near the bow area to suddenly rotate, overturn, or submerge, which in turn triggers rapid and intense increases in contact forces. Furthermore, when the contact angle of the ice changes sharply, local contact conditions become unstable, or the pack ice posture changes suddenly, the contact stiffness and reaction forces can increase rapidly, ultimately manifesting as pronounced impact peaks in the resistance curve.

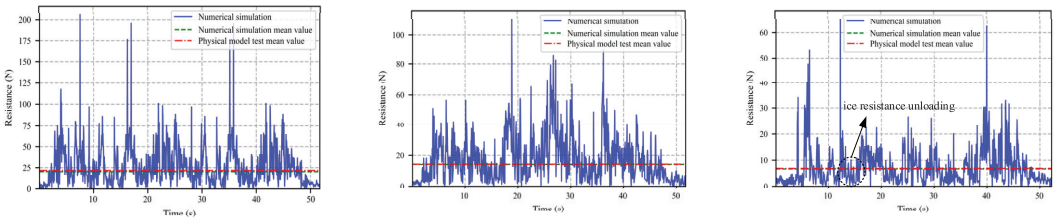

(a) 60% *(b) 45%* *(c) 30%*

Fig. 10. Ice resistance at 0.53 m/s for different ice concentrations

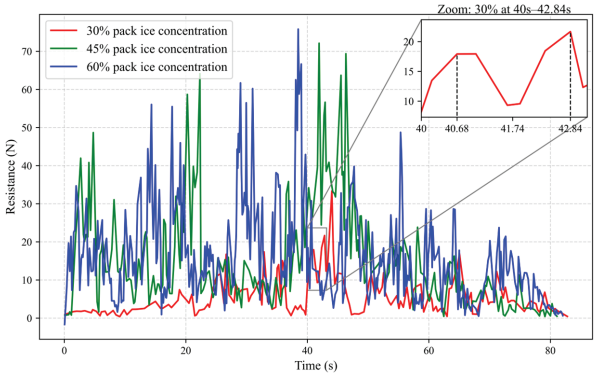

Fig. 12. Upper envelope of resistance at 0.33 m/s at varying ice concentrations

The curve fluctuations between 40 s and 42.84 s at 30% ice concentration shown in Fig. 12, based on the contact process between the ship bow and ice in both the numerical simulation and ship model test at a speed of 0.33 m/s (Fig. 13), illustrate that the ice near the bow is repeatedly compressed and slides along the hull, causing sudden surges and disturbances in resistance. Such phenomena are especially pronounced in high-density pack ice environments, where ship–ice contacts occur more frequently and interactions become more intense. This is manifested as more frequent redistribution, compression, and accumulation of ice in front of the bow, with strong nonlinear response behaviours.

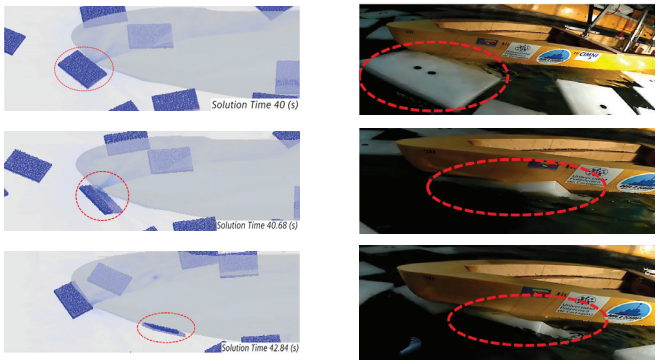

(a) Numerical simulations *(b) Ship model tests*

Fig. 13. Crushing of ice against the bow at 0.33 m/s and 30% ice concentration

DISTRIBUTION OF ICE LOAD ON THE BOW

To further investigate the influence of the ship's velocity on the distribution characteristics of contact loads in pack ice environment, numerical simulations were conducted under different velocity conditions. As shown in Fig. 14, for a pack ice concentration of 45%, the maximum contact forces recorded for the model ship were 514 N at 0.53 m/s, 242 N at 0.33 m/s, and 146 N at 0.22 m/s.

Significant variations were observed in the spatial distribution of the maximum contact forces in the bow region at different velocities, with a clear evolutionary pattern emerging with changes in the ship's speed. Overall, the spatial distribution of the bow's maximum contact force transitioned from a concentrated pattern to a more dispersed one, and from a symmetric distribution to an asymmetric one, with strong velocity-dependence and spatial evolution characteristics. These patterns reflect a shift in the impact modes of the ice and the contact mechanisms as a function of the ship's velocity.

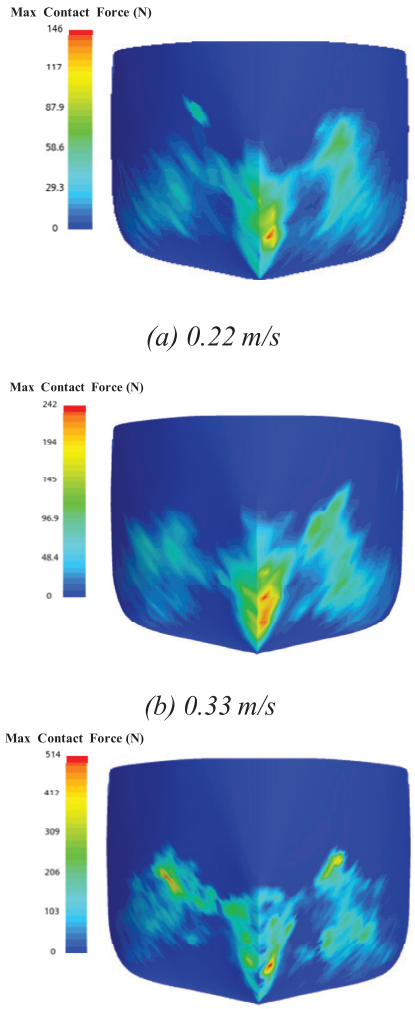

Fig. 14. Maximum contact force distribution on the ship model at 45% ice concentration

The results indicate that during navigation in pack ice conditions, the maximum contact force is concentrated at the bow, while significantly lower forces are observed along the sides of the ship. This poses a challenge in terms of structural integrity, particularly due to the potential for high stress concentrations in local hull regions. The contact force distribution clearly reveals a load concentration pattern resulting from the ice–ship interaction, providing a basis for structural reinforcement design.

REGIONAL RESISTANCE ANALYSIS

To further investigate the contributions of different hull regions to the total resistance during navigation, a decile division method was employed to analyse the hull resistance in detail. The hull was divided into sections along the transverse (beam) direction to enable a systematic evaluation of the local resistance distribution characteristics in each zone. This approach helped in gaining an understanding of the spatial distribution structure of resistance, and provides a reference for subsequent studies involving hull form optimisation, ice load structural layout, and propulsion system arrangement.

The maximum breadth B of the hull was divided symmetrically into 10 segments with equal width $\Delta B = B/10$ numbered B1–B10, where B1–B5 corresponded to the port side and B6–B10 to the starboard side, as shown in Fig. 15. This division was suitable for studying the uneven transverse distribution of pack ice effects.

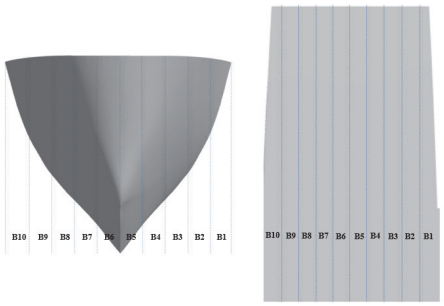

Fig. 15. Transverse sections of the hull (left: forward bow view; right: overhead stern view)

Fig. 16 shows the mean resistance distribution by region at an ice concentration of 45% and navigation speeds of 0.33 m/s and 0.53 m/s. According to the simulation results, the average transverse resistance on the hull at 0.53 m/s has a higher value in the midship area and lower values at the sides, whereas at 0.33 m/s, local elevations in resistance appear. Of the 10 regions, B5 has the highest mean resistance, followed by B6, representing the main loading areas of the hull's maximum breadth. The outermost regions on both sides, B1 and B10, have a higher mean resistance compared to their adjacent areas (e.g. B2 and B9). Combined with the maximum contact force distribution at the bow shown in Fig. 14, it is evident that regions B4 and B7 have both the lowest average contact force and the lowest mean resistance of all segments.

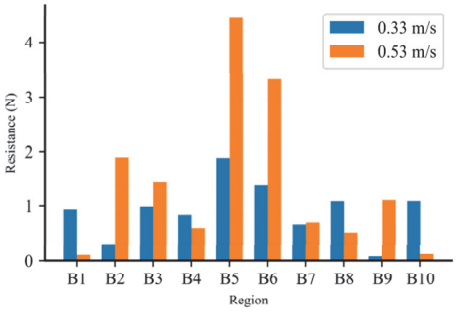

Fig. 16. Regional distribution of mean resistance

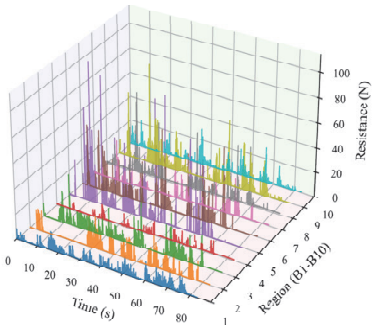

(a) Time history curves

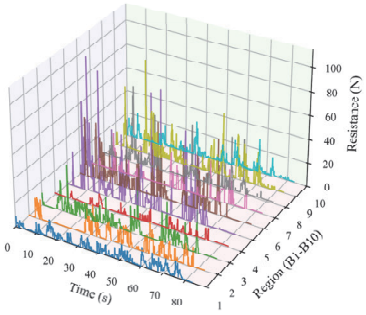

(b) Resistance–time history envelopes

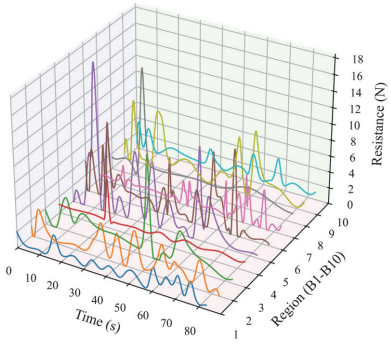

(c) Fitting of the time history curves

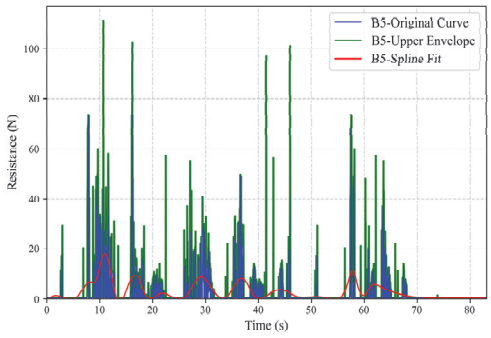

(d) Results for region B5

Fig. 17. Resistance curves for regions B1–B10 and region B5

Fig. 17 illustrates the ice resistance of each segment at a speed of 0.33 m/s. Fig. 17(a) shows the resistance, and Fig. 17(b) presents the upper envelope curves for the resistance in each segment. Fig. 17(c) displays the fitted curves for the resistance. Fig. 17(d) provides a detailed view of the curve variations in the B5 region. In general, the resistance in all segments exhibits intense non-stationary fluctuations, indicating frequent and uneven interactions between the hull and pack ice during navigation, characterised by high-impact and sudden load variations. In particular, the midship regions (e.g. B5 and B6) show significantly higher peak resistances and more frequent fluctuations compared to other segments, suggesting that the midship is the primary ice-loading area. This phenomenon also indicates that the bow region experiences the maximum ice load during vessel propulsion.

Moreover, several of the segment resistance curves show a rapid drop, in which a sharp decline follows immediately after a peak in resistance. This phenomenon reflects the ice resistance unloading mechanism, where pack ice, after exerting force on the hull through contact, suddenly slips or detaches from the surface, causing an instantaneous decrease in ice resistance on the hull.

CONCLUSION

This study has presented a high-precision method that combines image recognition with CFD–DEM and a 6-DOF model for the prediction of ship resistance in ice-covered waters. The watershed image segmentation algorithm and surface jetting were used to reconstruct ice distributions from test images, which greatly improved the consistency between the simulation and experiment.

In numerical simulations under different ice concentrations and speeds, the average error compared to the results of ship model tests was found to be within 10%. Compared with the traditional hydrodynamic simulation approach in which the ship is assumed to be stationary, the dynamic overset mesh and 6-DOF model strategy proposed in this study are better able to represent actual navigation conditions, thereby enhancing the physical realism and engineering applicability of the model.

A simulation analysis further revealed the nonlinear characteristics of ice resistance under the action of pack ice. It was found that the bow area, due to frequent collisions, accumulation, and slipping of pack ice, was the region with the highest contact force concentration and the main source of resistance. Meanwhile, the resistance distribution showed a pattern of decreasing values from the centre of the bow toward both sides of the hull. The resistance along the hull sides was significantly lower, with the average resistance and maximum contact force near the bow sides being the lowest over the entire hull, representing a typical localised load concentration feature.

In addition, at certain times or in local areas, slight increases in resistance appeared along the sides of the hull, which may be related to the skewed movement or sliding path changes of the pack ice. This distribution trend, from central concentration to side attenuation accompanied by local disturbances, provides important insights for structural design, indicating a need to reinforce the structural strength and impact resistance of the bow's central area while also paying attention to occasional load variations along the hull sides.

In summary, the numerical simulation method developed in this study effectively reproduced the complex ship–ice interaction processes in pack ice environments. The findings not only help to reveal the true mechanisms of hull loading but also provide essential technical support for the structural design of polar ships, optimisation of icebreaking performance, and management of navigation risk.

ACKNOWLEDGEMENTS

Funding agency:
supported by the Joint Program Project of Liaoning Provincial Science and Technology Program under Grant No. 2025-MSLH-079, the Fundamental Research Funds for the Central Universities" with grant No.3132025144, the Fundamental Research Funds for the Central Universities" with grant No. 3132025143, the "University Fundamental Research Project of the Education Department of Liaoning Province" with grant No. LJ212510151010.

REFERENCES

1. Stroeve JC, Notz D, Dawson J, Schuur EAG, Dahl-Jensen D, Giesse C. Disappearing landscapes: The Arctic at +2.7 °C global warming. Science 2025, vol. 387, no. 6734, pp. 616–621. https://doi.org/10.1126/science.ads1549

2. Gunnarsson B, Moe A. Ten years of international shipping on the Northern Sea Route: Trends and challenges. Arctic Review on Law and Politics 2021, vol. 12, pp. 4–30. https://www.jstor.org/stable/48710640

3. Petrov IV, Kharchilava KP, Pukhova MM, Bashkov DU, Shtanova KA. The Northern Sea Route in the system of international transport corridors as a logistic basis for the development of Arctic resources. IOP Conference Series: Earth and Environmental Science 2019, vol. 377, p. 012063. https://doi.org/10.1088/1755-1315/377/1/012063

4. Xu S, Kim E, Haugen S. Review and comparison of existing risk analysis models applied within shipping in ice-covered waters. Safety Science 2021, vol. 141, p. 105335. https://doi.org/10.1016/j.ssci.2021.105335

5. Li F, Huang L. A review of computational simulation methods for a ship advancing in broken ice. Journal of Marine Science and Engineering 2022, vol. 10, no. 2, p. 165. https://doi.org/10.3390/jmse10020165

6. Gutiérrez-Romero JE, Ruiz-Capel S, Esteve-Pérez J, Zamora-Parra B, Luna-Abad JP. Methodology based

on photogrammetry for testing ship-block resistance in traditional towing tanks: Observations and benchmark data. Journal of Marine Science and Engineering 2022, vol. 10, no. 2, p. 246. https://doi.org/10.3390/jmse10020246

7. Matala R, Suominen M. Investigation of vessel resistance in model scale brash ice channels and comparison to full scale tests. Cold Regions Science and Technology 2022, vol. 201, p. 103617. https://doi.org/10.1016/j.coldregions.2022.103617

8. Suominen M, Puolakka O. A new friction coefficient correction for ship model scale testing in brash ice channel. 27th IAHR International Symposium on Ice, Gdańsk, Poland, 2024.

9. Wan Z, Yuan Y, Tang W. Experimental investigation on ice resistance of an arctic LNG carrier under multiple ice breaking conditions. Ocean Engineering 2022, vol. 265, p. 113264. https://doi.org/10.1016/j.oceaneng.2022.113264

10. Lindqvist, G. A straightforward method for calculation of ice resistance of ships. Proceedings of the International Conference on Port and Ocean Engineering under Arctic Conditions (POAC), Lulea, Sweden, 12–16 June 1989; pp. 722–735.

11. Islam M, Mills J, Gash R, Pearson W. A literature survey of broken ice-structure interaction modelling methods for ships and offshore platforms. Ocean Engineering 2021, vol. 218, p. 108527. https://doi.org/10.1016/j.oceaneng.2020.108527

12. Kim MC, Lee SK, Lee WJ, Wang JY. Numerical and experimental investigation of the resistance performance of an icebreaking cargo vessel in pack ice conditions. International Journal of Naval Architecture and Ocean Engineering 2013, vol. 5, no. 3, pp. 457–468. https://doi.org/10.2478/IJNAOE-2013-0121

13. Huang L, Li F, Li M, Khojasteh D, Luo Z, Kujala P. An investigation on the speed dependence of ice resistance using an advanced CFD+DEM approach based on pre-sawn ice tests. Ocean Engineering 2022, vol. 255, p. 112530. https://doi.org/10.1016/j.oceaneng.2022.112530

14. Sawamura J, Tachibana T. Development of a numerical simulation for rotating and sliding of the ice floes along a ship hull. Proceedings of the 21st International Conference on Port and Ocean Engineering under Arctic Conditions (POAC'11); 2011 Jul 10–14; Montréal, Canada. Port and Ocean Engineering under Arctic Conditions (POAC); 2011. p. 1–10.

15. Xie C, Zhou L, Ding S, Liu R, Zheng S. Experimental and numerical investigation on self-propulsion performance of polar merchant ship in brash ice channel. Ocean Engineering 2022, vol. 269, p. 113424. https://doi.org/10.1016/j.oceaneng.2022.113424

16. Zhang J, Zhang Y, Shang Y, Jin Q, Zhang L. CFD-DEM based full-scale ship-ice interaction research under FSICR ice condition in restricted brash ice channel. Cold Regions Science and Technology 2021, vol. 192, p. 103454. https://doi.org/10.1016/j.coldregions.2021.103454

17. Tang X, Zou M, Zou Z, Li Z, Zou L. A parametric study on the ice resistance of a ship sailing in pack ice based on CFD-DEM method. Ocean Engineering 2022, vol. 258, p. 112563. https://doi.org/10.1016/j.oceaneng.2022.112563

18. PolarIN. BIO Hesperides ES. EU Polar Research Infrastructure Network. Retrieved October 15, 2025, from https://eu-polarin.eu/bio-hesperides-es/#.

19. Li H, Feng Y, Ong MC, Zhao X, Zhou L. An approach to determine optimal bow configuration of polar ships under combined ice and calm-water conditions. Journal of Marine Science and Engineering 2021, vol. 9, no. 6, p. 680. https://doi.org/10.3390/jmse9060680

20. Tsuji T, Tanaka S, Ishida T. Lagrangian numerical simulation of plug flow of cohesionless particles in a horizontal pipe. Powder Technology. September 1992, vol. 71, no. 3, pp. 239–250. https://doi.org/10.1016/0032-5910(92)88030-L

21. Detert M, Weitbrecht V. User guide to gravelometric image analysis by BASEGRAIN. In Fukuoka S et al. (Eds.), Advances in river sediment research. London: Taylor & Francis Group; 2013. ISBN: 978-1-138-00062-9

22. Bowditch N. The American practical navigator, Chapter 32: Ice navigation. US Naval Oceanographic Office, 2017. Retrieved from https://thenauticalalmanac.com/2017_Bowditch-_American_Practical_Navigator/Volume-_1

23. CCG. Ice navigation in Canadian waters(7th edition). Canadian Coast Guard, Minister of Fisheries and Oceans: Ottawa, ON, Canada, 2025. Retrieved from: https://www.ccg-gcc.gc.ca/publications/icebreaking-deglacage/ice-navigation-glaces/page01-eng.html

24. Huang Y, Li W, Wang Y, Wu B. Experiments on the resistance of a large transport vessel navigating in the Arctic region in pack ice conditions. Journal of Marine Science and Application 2016, vol. 15, no. 3, pp. 269–274. https://doi.org/10.1007/s11804-016-1362-x.